12-12-2021

Conductive Stimuli-Responsive Coordination Network Linked with Bismuth for Chemiresistive Gas Sensing

Aylin Aykanat
Dartmouth College

Christopher G. Jones
California Institute of Technology

Evan Cline
Dartmouth College

Robert M. Stolz
Dartmouth College

Zheng Meng
Dartmouth College

See next page for additional authors

Follow this and additional works at: https://scholars.unh.edu/nh_epscor

Comments

Recommended Citation

Authors

Aylin Aykanat, Christopher G. Jones, Evan Cline, Robert M. Stolz, Zheng Meng, Hosea M. Nelson, and Katherine A. Mirica

Conductive Stimuli-Responsive Coordination Network Linked with Bismuth for Chemiresistive Gas Sensing

Aylin Aykanat, Christopher G. Jones, Evan Cline, Robert M. Stolz, Zheng Meng, Hosea M. Nelson,* and Katherine A. Mirica*

ACCESS | Metrics & More | Article Recommendations | Supporting Information

ABSTRACT: This paper describes the design, synthesis, characterization, and performance of a novel semiconductive crystalline coordination network, synthesized using 2,3,6,7,10,11-hexahydroxytriphenylene (HHTP) ligands interconnected with bismuth ions, toward chemiresistive gas sensing. Bi(HHTP) exhibits two distinct structures upon hydration and dehydration of the pores within the network, Bi(HHTP)-α and Bi(HHTP)-β, respectively, both with unprecedented network topology (2,3-c and 3,4,4,5-c nodal net stoichiometry, respectively) and unique corrugated coordination geometries of HHTP molecules held together by bismuth ions, as revealed by a crystal structure resolved via microelectron diffraction (MicroED) (1.00 Å resolution). Good electrical conductivity (5.3 × 10^{-3} S·cm^{-1}) promotes the utility of this material in the chemical sensing of gases (NH$_3$ and NO) and volatile organic compounds (VOCs: acetone, ethanol, methanol, and isopropanol). The chemiresistive sensing of NO and NH$_3$ using Bi(HHTP) exhibits limits of detection 0.15 and 0.29 parts per million (ppm), respectively, at low driving voltages (0.1−1.0 V) and operation at room temperature. This material is also capable of exhibiting unique and distinct responses to VOCs at ppm concentrations. Spectroscopic assessment via X-ray photoelectron spectroscopy (XPS) and Fourier transform infrared spectroscopic methods (i.e., attenuated total reflectance-infrared spectroscopy (ATR-IR) and diffuse reflectance infrared Fourier transformed spectroscopy (DRIFTS)), suggests that the sensing mechanisms of Bi(HHTP) to VOCs, NO, and NH$_3$ comprise a complex combination of steric, electronic, and protic properties of the targeted analytes.

KEYWORDS: bismuth, coordination network, chemiresistor, crystalline, gas sensor, microelectron diffraction, semiconductive
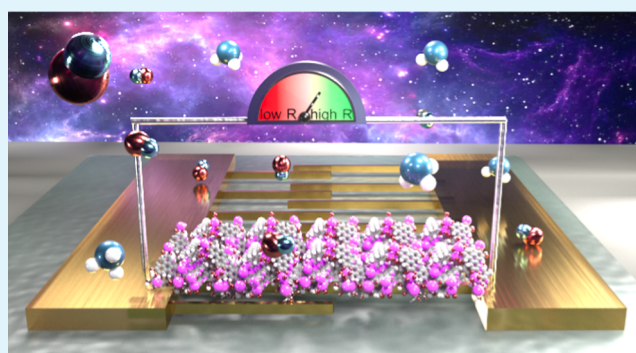
INTRODUCTION

In today's densely inhabited society, there is an increasing need for the design and synthesis of new materials for low-power portable gas sensors with potential applications in monitoring atmospheric pollution,[1,2] home and work safety,[3,4] filtration of air for personal safety,[5] and breath diagnostics.[6] Full realization of these applications would significantly benefit from the design and fabrication of low-cost, low-power wireless gas sensors that do not rely on expensive equipment or trained technicians for analysis.[7] Nanomaterial-based chemiresistive sensors offer a unique approach toward this goal, with vast potential for addressing the increasing demand of portable sensors in environmental and healthcare applications.[8] Primary demonstrations of nanomaterial-based sensors, such as those fabricated from metal oxides,[9] carbon nanotubes (CNTs),[10] and synthetically modified graphene,[11] have confirmed the value of nanostructured materials in terms of high sensitivity,[12] low power consumption,[13] and rapid response time.[14] Yet specific limitations, such as ambiguity of sensing mechanisms, selectivity to analytes, and cost-effectiveness of device

integration methods, limit the practical applications of nanomaterial-based sensors.[15]

Crystalline conductive coordination polymers (CPs), such as metal−organic frameworks (MOFs)[16] and coordination networks (CNs),[17] offer a promising alternative as a new emerging class of materials with broad applicability in chemiresistive detection.[18−25] High conductivity and tunable surface chemistry, combined with modular porosity and high surface area for gas uptake—all accessible through bottom-up self-assembly—give this class of materials a set of unique attributes that are particularly well suited for applications in gas sensing.[18,19,23,26] Despite this promise, most conductive coordination polymers that have thus far been employed in chemical sensing have two significant shortcomings. First, they
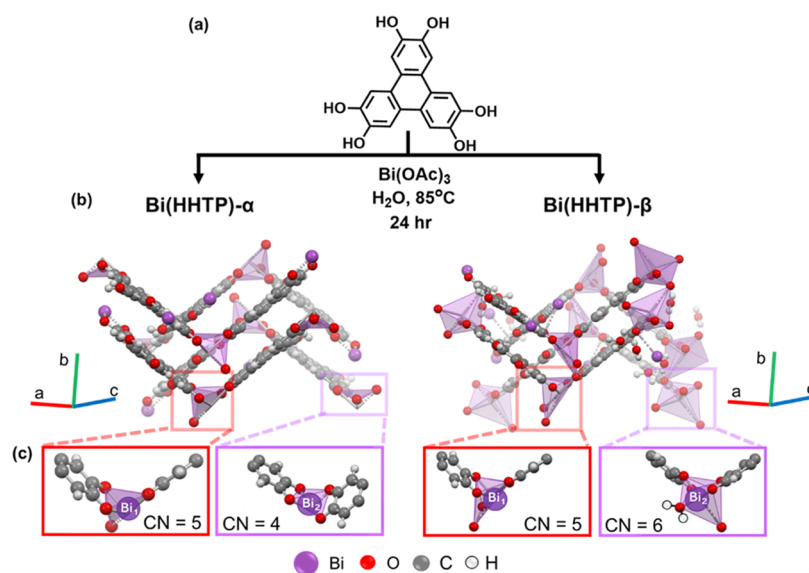
Figure 1. (a) General reaction scheme and (b) structure of Bi(HHTP)-α and Bi(HHTP)-β. (c) Coordination polyhedral around two nonequivalent coordination polyhedra of Bi(HHTP)-α and Bi(HHTP)-β. In Bi(HHTP)-α, Bi$_2$ is displayed as a distorted tetragonal pyramid (CN = 5) and Bi$_1$ is shown as a distorted quadrilateral (CN = 4). In Bi(HHTP)-β, Bi$_1$ is displayed as a distorted pentagonal pyramid (CN = 5) and Bi$_2$ as a distorted one-capped octahedron (CN = 6).

are based on two-dimensional (2D) lattices comprising first-row transition metals with square planar or octahedral coordination geometries around the metal site.[16,18,20,21,23−25,28−31] While these low-dimensional materials exhibit high sensitivity to small reactive gases and vapors, the reliance on 2D lattices fundamentally limits gains in selectivity that can be achieved through stereoelectronic tuning of a binding site with a more complex coordination geometry. To address this fundamental limitation, we reasoned that expanding beyond first-row transition metals to create conductive networks with complex topologies and new, unsaturated coordination environments may promote gains in selectivity through simultaneous tuning of steric and electronic attributes of intermolecular interactions of sensing materials with analytes. The use of bismuth ions within a coordination network can enable solutions to these limitations by allowing tailoring of multiple useful and functional properties, such as charge delocalization and a tunable coordination environment. Additionally, flexible coordination sites capable of undergoing analyte-induced changes within the the coordination environment can provide room to investigate the contributions of structural features in relation to sensing within a well-ordered material. Furthermore, the advantages of utilizing microED can help overcome the challenges associated with obtaining suitably large crystallites of 2D framework materials, where the lack of single-crystal diffraction studies in established framework systems conceals structural information and characterization studies. This limitation restricts the fundamental understanding of the interactions of host framework materials with guest analytes.[24]

MOLECULAR DESIGN

The molecular design of the conductive coordination network capitalizes on several unique characteristics of bismuth-containing compounds and materials and extends these characteristics to generate a new material with promising functionality. Currently, bismuth-based materials and coordination compounds have applications in healthcare,[32] photo-catalytic function,[33,34] radiation technology,[35] and gas adsorption and storage.[36] The unique flexible coordination sphere of bismuth,[37] Lewis acidity,[38] nontoxicity,[39] stability,[40] as well as the high affinity for soft and hard ligands, enable desirable structure−property relationships,[41] particularly when bismuth is used as a constituent within CPs.[42] Specifically, bismuth-based CPs[43] and porous metal−organic frameworks (MOFs)[44] have demonstrated valuable structure−property relationships, such as conductivity[43,45] and photocatalysis.[33] These properties are tunable through the strategic selection of constituent organic linkers in bismuth-containing CPs that can dictate the coordination environment around the bismuth metal node.[43]

The unique nature of bismuth-based coordination networks allows for the tailoring of multiple useful and functional properties, such as charge delocalization,[45,46] band gap, and direction of assembly, or dimensionality through careful selection of organic ligands.[43] Several of these properties are highly desirable in the context of chemiresistive sensing. First, conductive CPs may be designed by selecting constituents that contain loosely held valence shell electrons and ligands that permit their efficient through-bond charge delocalization,[17,43] allowing the integration of the semiconductive material into amperometric devices for chemical sensing. This charge delocalization has been well documented within both bismuth oxide lattices[47] and bismuth-based metal−organic coordination networks.[45,46] Second, the flexible coordination geometry of bismuth provides control over dimensionality of the coordination network structure,[43] resulting in unique structure−property relationships through ligand modification strategies and through the choice of bismuth metal salt. Third, the structures of Bi(III)-containing compounds often present a vacant or flexible coordination site at the bismuth center, which may serve as an electron acceptor site.[40,43] The coordination environment around the bismuth ion may undergo further interaction with analytes, thereby enabling selective chemical detection of analytes with a three-dimensional (3D) coordination sphere of bismuth accompanied by
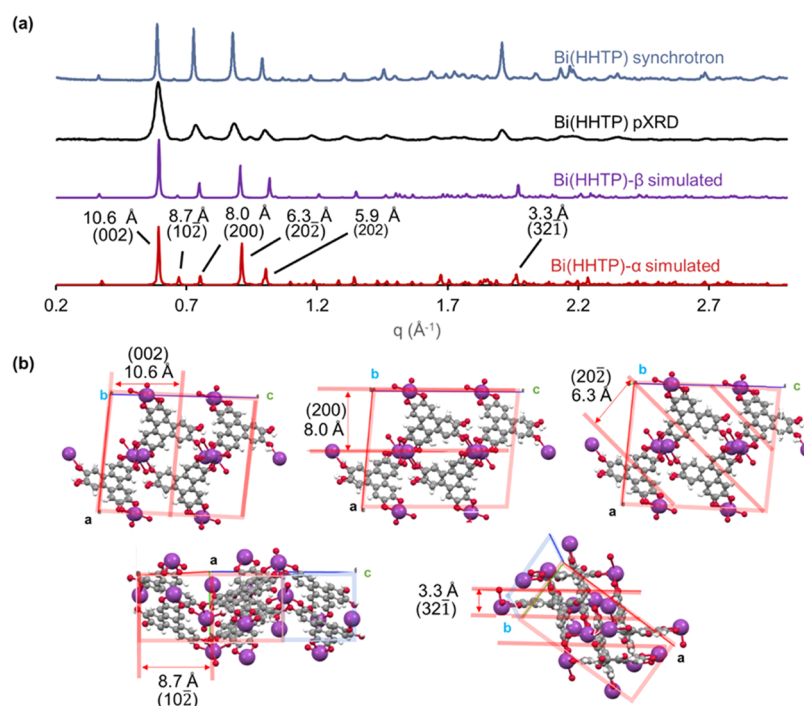
Figure 2. (a) Experimental and simulated MicroED pXRD patterns of Bi(HHTP)-α and (b) corresponding (002), (20$\bar{2}$), (200), (10$\bar{2}$), and (32$\bar{1}$) crystalline planes and interatomic distances.

electronic transduction of signal. Capitalizing on these advantages can provide a path to control these functional properties in selective chemical sensing.

Our molecular design is inspired by previously reported literature of bismuth-based semiconductive coordination networks interconnected with triphenylene-based ligands.[46] The precedent set by Li et al. utilized hexakis(alkylthio)-triphenylene (alkyl: methyl, ethyl, and isopropyl) triphenylenes reacted with bismuth halides to produce semiconductive hybrid networks that featured flexible network dimensionalities and tunable electronic properties.[43] We reasoned that substituting the alkylthio substituents with hydroxy groups may promote similar coordination chemistry with bismuth ions while generating a material with good stability to water and air due to the robust nature of hydroxy-substituted triphenylenes and the strong nature of Bi−O bonds,[48] compared to their sulfur substituted analogues. The 2,3,6,7,10,11-hexahydroxy-triphenylene (HHTP) ligand exhibits a large π-conjugated system and threefold symmetry (Figure 1) and has previously been reported to form conductive metal−organic frameworks using first-row transition metals[21,23,25] and lanthanides.[49]

A useful attribute of HHTP and HHTP-based MOFs is that they can undergo electron-transfer interactions that can be coupled to proton-transfer events.[50] This colocalized ability to interact with analyte protons and electrons using HHTP may provide an additional level of selectivity in sensing devices for protic guests. Despite the useful properties displayed by HHTP, CPs employing this ligand are unprecedented for metal complexes with bismuth. We aimed to achieve bottom-up assembly of a conductive CP that provides a three-dimensional (3D) ligand coordination environment around the metal center tailored for enhanced selectivity in response to specific gas-phase molecules. Thus, we subjected bismuth (III) acetate to aqueous reaction conditions and paired this node with a polyaromatic organic linker to observe a dark green micro-

crystalline powder. Bi(HHTP) exhibited distinct structural transformations upon dehydration and hydration of the pores within the network (here termed Bi(HHTP)-α and Bi-(HHTP)-β, respectively), likely driven by hydrogen-bonding interactions with the oxo groups on the ligand, which induced changes in the coordination environment of both bismuth centers and unit cell parameters. This type of dynamic flexibility, such as the slipping and/or expansion of the layers, has been previously investigated in 2D HHTP-based MOFs using quantum mechanical calculations.[51]

EXPERIMENTAL PROCEDURE

Synthesis and Characterization. We used hydrothermal synthesis that combined Bi(OAc)$_3$ and HHTP to produce Bi(HHTP) (Figure 1). Reaction optimization procedures carried out after powder X-ray diffractometry (pXRD) analysis revealed the presence of residual starting material Bi(OAc)$_3$, when Bi(HHTP) was synthesized using a 2:1 molar ratio of Bi(OAc)$_3$ and HHTP (see Figure S5). This residual starting material can be removed with a purification procedure (overnight stirring in H$_2$O at 50 °C) followed by subsequent washes with ethyl acetate (see Section 1 in the Supporting Information (SI)), or a Soxhlet extraction technique using ethyl acetate (only effective using small scale synthesis, see Section 1 of the SI). Residual Bi(OAc)$_3$ starting material can be avoided altogether through the use of a stoichiometric 1:1 molar ratio of Bi(OAc)$_3$ and HHTP (see Section 1.4 in the SI). The resulting dark green/blue conductive, microcrystalline powder [Bi(HHTP)] was initially characterized using pXRD analysis (Figure 2), scanning and transmission electron microscopy (SEM and TEM, respectively), and elemental analysis. The experimental pXRD pattern of Bi(HHTP) exhibited a high-intensity peak in the low-angle range at 8.36° 2θ. This peak corresponds to an interatomic distance of 10.6 Å and the (002) plane, which bisects the unit cell of Bi(HHTP) (Figure 2).

Other major peaks appearing in the pXRD pattern included the (10$\bar{2}$), (200), (20$\bar{2}$), (202), and (32$\bar{1}$) planes, which were attributed to interatomic distances of 8.7, 8.0, 6.3, 5.9, and 3.3 Å using Bragg's law, respectively. The (002) and (20$\bar{2}$) planes intersected a section of
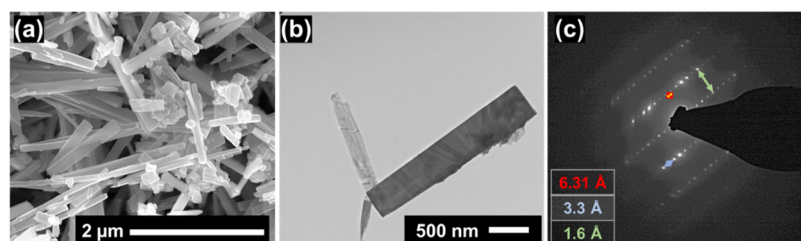
Figure 3. (a) Scanning electron micrograph (SEM), (b) transmission electron micrograph (TEM), and (c) selected area electron diffraction of Bi(HHTP).

one HHTP ligand when viewed along the crystallographic c-axis, while the (200) and the (10$\bar{2}$) planes intersected and ran parallel to the bismuth atoms (Figure 2b). The (32$\bar{1}$) crystalline plane runs parallel to the π–π stacking distance and corresponds to an interatomic distance of 3.3 Å. We contribute the slight offset of the (32$\bar{1}$) peak to the limitations in resolution of microED and the highly disordered solvent present within the void space of the Bi(HHTP)-β structure, which could have affected the layering of π–π stacking planes. For higher-resolution crystal structure analysis, Bi(HHTP) material was analyzed using a synchrotron light source at Argonne National Laboratories (Beamline 11-BM) (Figure 2a).

RESULTS AND DISCUSSION

Morphological characterization of Bi(HHTP) *via* SEM analysis revealed rectangular-shaped crystallites of varying lengths (Figure 3a). TEM imaging, obtained after 1.0 mg of Bi(HHTP), was sonicated in acetone for 16 h and dropcasted onto a carbon grid, provided visualization of rectangular, sheetlike materials (Figure S9). Further characterization of Bi(HHTP) using TEM analysis revealed the presence of a distinct crystallite with a length of ~2 μm (Figure 3b). Selected area diffraction analysis (SAED) on this crystallite showed well-ordered diffraction spots in reciprocal space (Figure 3c), which we used as a complementary method of measuring interatomic distances along diffraction planes. The distances between the diffraction spots were calculated according to the equation derived from Bragg's law (eq S1). Two interatomic distances (3.3 and 6.3 Å) measured within the SAED nanocrystal were also present in the pXRD pattern (Figure 2). The 6.3 Å distance observed in the nanocrystal was slightly offset in the pXRD (6.6 Å) and likely corresponded to the (20$\bar{2}$) *hkl* plane, while the 3.3 Å interatomic distance corresponded to the (32$\bar{1}$) plane, which is parallel to π–π stacking distances (Figure 2b).

Although Bi(HHTP) displayed high crystallinity, efforts to grow a single crystal large enough for single-crystal X-ray diffraction (SCXRD) using methods such as slow evaporation, high pressure/temperature synthesis, and slow addition techniques were unsuccessful; thus, we focused our attention on microelectron diffraction (MicroED).[52] Although the MicroED method was popularized by structural biologists for the characterization of proteins, this technique has proven invaluable for the field of small-molecule characterization,[52] and even more recently, the characterization of both coordination networks and MOFs.[53] MicroED enabled the structural characterization of Bi(HHTP) and permitted the correlation of the *hkl* planes in this structure to the ones observed in the experimental pXRD spectrum (Figure 2).

Analysis of Crystallographic Structure from MicroED. For MicroED analysis, electron diffraction data was collected using a Talos F200C transmission electron microscope equipped with a Thermo-Fischer CetaD detector. To prepare

sample grids (quantifoil or pure carbon TEM grids), a TEM grid was placed in a vial containing dry powder and gently shaken. Images were collected in a movie format as crystals were continuously rotated under a focused electron beam. Typical data collection was performed using a constant tilt rate of 0.3°/s between the minimum and maximum tilt ranges of −72° to +72°, respectively (see the SI for details). Structural characterization by MicroED revealed that Bi(HHTP) exhibited two distinct structural forms, Bi(HHTP)-α and Bi(HHTP)-β, respectively. Bi(HHTP)-α exhibited monoclinic (α, γ = 90°, β = 94°) type Bravais lattice with symmetry group P2₁/c and intricately connected layers (*vide infra*). Bi(HHTP)-β displayed different cell parameters (α, γ = 90°, β = 97°), occupied pores (likely water molecules from incomplete drying), and distinct coordination geometries, but the same symmetry group, P2₁/c (Figure S7). Pawley refinement was conducted using the crystallographic information file (cif) obtained from MicroED for Bi(HHTP)-α, which provided unit cell parameters and presented a R_{wp} of 7.07% and a R_p of 12.54% (see Section 3 in the SI).

Topological analysis performed using a ToposPro program package[54,55] and the Topological Types Database (TTD) collection of periodic networks was used to determine the network topology model in the coordination network (Section 2 in the Supporting Information). The topological description includes a simplification procedure (graph theory approach), which was used to describe the crystal net topology and designate a 2,3-C4 topological type net for Bi(HHTP)-α, which corresponds to this structure in its standard representation (Figure S15). The cluster simplification procedure was also implemented to identify more complex building units of a structure and characterize their connection mode, where the fragments of Bi(HHTP)-α form infinite chains linked through Bi−O linkages (Figure S19b) and exhibit rod packing with 2M4-1 topology and point symbol {4}.[55]

The Bi(HHTP)-α sheet contains dimeric one-dimensional (1D) zigzagging chains of alternating nonplanar HHTP ligands that connect one 1D chain to another through the longest Bi₁−O bond of 2.6 Å. These dimeric chains contain alternating uncoordinated semiquinone groups and stack in the crystallographic b-direction through π−π stacking interactions. Binding interactions present inside one-dimensional chains connecting HHTP constituents are approximately 4.1 Å long. Both Bi(HHTP)-α and -β adopt a herringbone-like packing motif, similar to HHTP (see Section 1 in the SI),[56] where bismuth ions cause distortions in the π−π stacking of the matrix through catechol bidentate chelation and slight rotation within the coordination sphere. Compared to bismuth-based MOFs made using carboxylate ligands, which exhibit Bi−O bond lengths ranging from 2.2 to 3.0 Å,[44] we observed a smaller
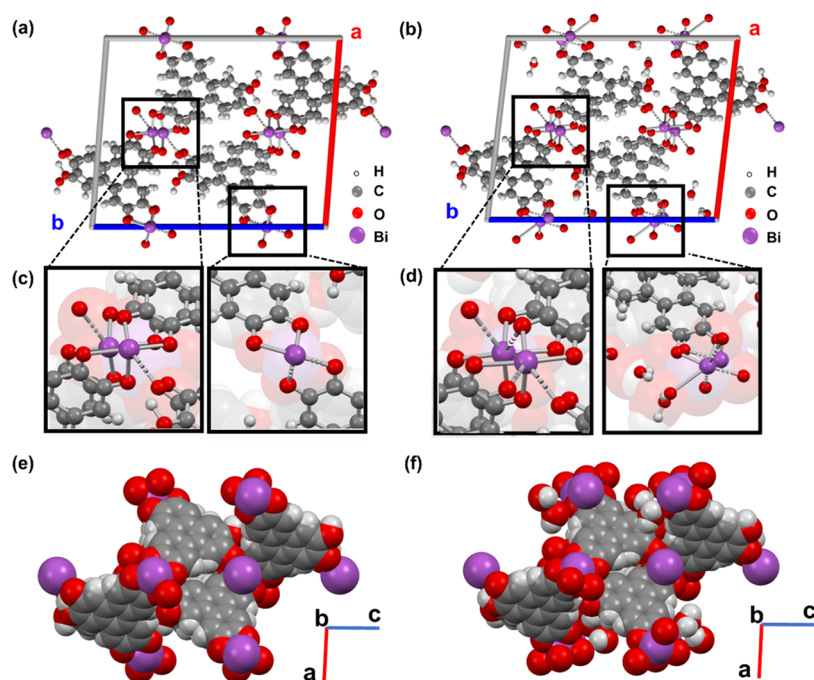
Figure 4. (a) Bi(HHTP)-α and (b) Bi(HHTP)-β structure within one unit cell view down the crystallographic b-axis. (c) Inset of Bi(HHTP)-α depicting coordination environments Bi$_1$ (left) and Bi$_2$ (right). (d) Inset of Bi(HHTP)-β depicting a new coordination environment of Bi$_1$ (left) and Bi$_2$ (right) after hydration. (e) Space-filling model of Bi(HHTP)-α and (f) Bi(HHTP)-β.

array of bond lengths, 2.0−2.6 Å, commonly seen in bismuth catecholate coordination. The $\pi-\pi$ stacking distance in Bi(HHTP)-α was measured at 3.3 Å, which matches the interatomic distance obtained from diffraction peaks in pXRD. Bi(HHTP)-α displays two coordination environments (Figure 1c), distorted tetragonal pyramid (Bi$_2$) and distorted quadrilateral (Bi$_1$); the latter is similar to a dimeric bismuth(III) catecholate coordination complex involved in a five-coordination environment reported previously.[57] Bi(HHTP)-β exhibited two distinct bismuth coordination spheres with six- and five-coordinate environments; the former (Bi$_2$) contains an aqua ligand (Figure 4d). Specifically, the coordination polyhedra of Bi$_1$ and Bi$_2$ contain a distorted pentagonal pyramid (CN = 5) and distorted one-capped octahedron (CN = 6), respectively.

We hypothesize that Bi(HHTP)-β hydrate was stabilized when water occupies the slitlike pores of the network (Figure 4b), altering unit cell parameters and permitting further interaction of each oxygen heteroatom in HHTP to neighboring layers. After hydration, bismuth containing CN = 4 in Bi(HHTP)-α shifted from an eclipsed environment, with respect to other bismuth atoms in adjacent layers, to a staggered conformation due to oxygen now in proximity within the pores of Bi(HHTP)-β (Figure 4). The presence of uncoordinated hydroxy groups facing inward within the pores (present in both structures) is likely further stabilized through hydrogen bonding (H-bonding) with the water molecules in Bi(HHTP)-β.

Additional Physical and Chemical Characterization.
IR Analysis. Attenuated total reflectance infrared spectroscopy (ATR-IR) of Bi(HHTP) revealed the presence of vibrational bands (Figure S21) at 1420 and 1157 cm^{-1}, which are characteristic of catechol vibrational modes.[58] Because the vibrational modes strongly depend on atomic masses, heavy bismuth ions should present vibrational bands at lower

frequencies (500−100 cm^{-1}). Thus, the appearance of new bands in this region may also be attributed to new Bi−O bond vibrational frequencies.

Surface Area Analysis. Structural characterization of the specific surface area of activated and degassed (at 85 °C and 635 Torr for 24 h) Bi(HHTP) using Brauner−Emmet−Teller (BET) analysis was performed using N$_2$ adsorption−desorption isotherms, collected at 77 K on a Micromeritics 3FLEX instrument. Preliminary results indicated a surface area of 26.8 m^2 g^{-1} (Figure S22). The low surface area measured from BET analysis using nitrogen (probe radius of 1.8 Å) is reasonable when compared to the accessible solvent surface area calculated using Materials Studio software, where a probe radius of 1.2 Å calculated a surface area 101.6 Å^2 and a free volume of 22.62 Å^3 (Figure S20).

Elemental Composition. Elemental microanalysis and inductively coupled plasma mass spectrometry (ICP-MS) confirmed the elemental composition of Bi(HHTP) (Table S2). The percent mass of carbon, hydrogen, and bismuth observed experimentally within the coordination network were 38.3, 1.51, and 33.1%, respectively. These values were closer in value to the percent mass theoretical calculations (39.0, 1.62, and 37.7%, respectively) based on the empirical formula of Bi(HHTP)-β (($C_{36}H_{12}O_{12}$)Bi$_2$·2(H$_2$O)), relative to the empirical formula for Bi(HHTP)-α (($C_{36}H_{12}O_{12}$)Bi$_2$), whose theoretical masses yielded values for carbon, hydrogen, and bismuth are 41.1, 1.51, and 39.4%, respectively. This comparison suggests the prevalence of the Bi(HHTP)-β structure within the sample, although the percent volume ratio of the two structures may fluctuate depending on drying conditions and can be further investigated using systematic thermal gravimetric analysis (TGA) analysis or statistical microED techniques.

Thermal Analysis. The thermal gravimetric analysis (TGA) profile of Bi(HHTP) revealed a total of ∼34% weight loss with

the highest rate of decomposition occurring at 466 °C (Figure S23). There was an initial mass loss of ∼8% from 100 to 200°C, potentially due to the loss of volatile solvent molecules such as acetone or H_2O, which is consistent with the presence of Bi(HHTP)-β or the hydration of the material. We observed a similar mass loss for Bi(OAc)$_3$ (38%) and a higher mass loss for the organic linker, HHTP (56%).

Analysis of the Oxidation State. X-ray photoelectron spectroscopy (XPS) enabled the analysis of bismuth in a low (3+) valence oxidation state through emission lines at binding energies of 160.1 and 165.3 eV, assigned to Bi^{3+} 4f$_{7/2}$ and Bi 4f$_{5/2}$ (see Section 3 in the SI).[59] We were unable to fully deconvolute the region of the O 1s primary emission line present at 532 eV to assign C−O and C═O bonds, due to the likely presence of H_2O both within the pores of the network and within the coordination sphere of Bi(HHTP)-β creating uncertainty around the correct electronic state of the ligand. Based on the deconvoluted primary C 1s emission line (Figure S25b) and considering the presence of Bi^{3+}, one possible oxidation state of the ligand to result in an overall neutral coordination network is a bis-semiquinone catechol state (sq, sq, cat) to generate Bi^{3+} within the network (Figure S25d). The C 1s spectra were consistent with this oxidation state, as they present C−O, C═O, and C−OH bonds in 2:2.6:1 ratio. Another possibility that renders a neutral framework is that bismuth atoms within the network are in a ratio of Bi^{3+}/Bi^{2+} oxidation state. These two oxidation states of HHTP generate an alternating (sq, sq, sq) and (sq, sq, cat) state (Figure S26b,c) and would generate a −2.5-overall charge on the ligand. This network structure would also create a radical ion on HHTP, which is plausibly what we are observing in electron paramagnetic resonance (EPR) spectroscopy (Section 4 in the SI).

Electronic Properties. Conductivity measurements of Bi-(HHTP) were performed using a four-point probe technique, which required 100 mg of material pressed into 6 mm diameter pellet of 0.2 mm thickness. Bi(HHTP) showed a bulk conductivity of 5.3×10^{-3} S·cm^{-1} (Section 3 in the SI, eq S2). Pellets of the precursors Bi(OAc)$_3$ and HHTP exhibited no measurable conductivity using a two-point probe digital multimeter (Extech EX430 series), which had a maximum resistance limit of measurement at 40 MΩ.

To investigate the Arrhenius activation energy for electrical conductivity of Bi(HHTP), a two-point probe on a 50 mg pressed pellet was employed to collect the current change under different temperatures (25−110 °C) with a linear sweep voltage from −2.0 to 2.0 V (Figure S24). The activation energy determined by this method was 425 meV. The optical band gap was determined by plotting the absorbance squared vs energy (eV) and estimated to be 1.61 eV based on the value of the absorption edge (Figure S28). Density functional theory (DFT) calculations were performed on the simulated structure of Bi(HHTP) using functional Perdew−Burke−Ernzerhof (PBE) and generalized gradient approximation (GGA) approximations (Figure S29). The high symmetry points in the first Brillouin zone demonstrated that the Dirac bands approached the Fermi level through the Y-A and E-C (crystallographic c) directions, where a low band gap of approximately 0.1 eV was observed for Bi(HHTP)-α and 0.08 eV for Bi(HHTP)-β. The partial density of states analysis showed that, compared with bismuth, the p orbitals from the C and O atoms contribute significantly to the Dirac bands.

Chemiresistive Gas Sensing. We hypothesized that Bi-(HHTP) would be a promising chemiresistive sensing material due to its flexible coordination sphere around the bismuth metal center, which may act as a potential binding site and accommodate gaseous probes, causing a direct perturbation of the charge transport with the semiconductive network. There is also the presence of free, uncoordinated hydroxy groups in both Bi(HHTP)-α and Bi(HHTP)-β that can promote H-bonding interactions in the vicinity of the bismuth atom. To characterize the fundamental ability of Bi(HHTP) to sense small reactive gases through electronic doping interactions, we examined the chemiresistive responses of Bi(HHTP) toward both oxidizing (NO) and reducing (NH$_3$) gaseous analytes. To further probe Bi(HHTP)'s capacity to detect analytes through a combination of electronic doping and H-bonding inter-actions, we also examined the response of Bi(HHTP) toward a range of H-bond donors (MeOH, EtOH, iPrOH) and H-bond acceptors (acetone).

To carry out the sensing procedure, we dropcasted 10 μL of a Bi(HHTP) suspension (1−2 mg/mL in H_2O) onto five devices containing interdigitated 10 μm gap gold electrodes, which generated devices with resistances in ∼30 MΩ range (see the SI, Section 4 for details). Since the suspension of Bi(HHTP) used for device fabrication was sonicated in H_2O and dried 16 h in ambient air, we hypothesize that the Bi(HHTP)-β structure was the dominant form within the devices. Furthermore, due to the similar band gaps of the α and β structures (Figure S29) and simulated XRD patterns (Figure 2a), we do not believe that the differences in the structures could lead to considerable differences in chemiresistive response. The devices were dried overnight in ambient air and then placed into an edge connector, wired to a breadboard and potentiostat (PalmSens) that applied 1.0 V voltage at room temperature. The devices were then enclosed in a Teflon chamber with gas inlet/outlet ports connected to Smart-Trak mass flow controllers delivering target concentrations of gases from premixed tanks purchased from AirGas (tanks of 10 000 ppm of NH$_3$ in N$_2$ and 10 000 ppm of NO in N$_2$). The concentrations of gaseous analytes were modified by adjusting flow rates (N$_2$ as the balance/purging gas). Generally, five devices at a time were exposed to each gas at different concentrations (5−1000 ppm) of the chosen analyte at a N$_2$ flow rate of 0.5 L/min and then purged with dry N$_2$ to examine Bi(HHTP)'s recovery.

For volatile organic compound (VOC) sensing, a Kintek FlexStream gas generator was used to produce vapors of the analyte (EtOH, MeOH, acetone, or iPrOH), which was diluted in N$_2$ (4 L/min) to the desired concentration. Each organic vapor was calibrated before use in the generator by heating the internal permeation glass chamber/tube, loading a vial of the desired VOC inside the tube and setting the span flow rate at for N$_2$ at 4 L/min (see Section 4.7 in the Supporting Information). Notably, we observed that altering flow rates between analytes affects the response of the material, where higher flow rates are used to deliver lower concentrations; thus, we chose to keep the flow rate constant and vary the rate of evaporation of the analyte through the control temperature within the vapor generator to acquire concentration-dependent experiments (eq S10). In all sensing measurements, the devices were kept at ambient temperature.

Chemiresistive Sensing Response. Although many examples of MOF-based sensors exist, to the best of our knowledge, this report constitutes the first example of bismuth-based CP
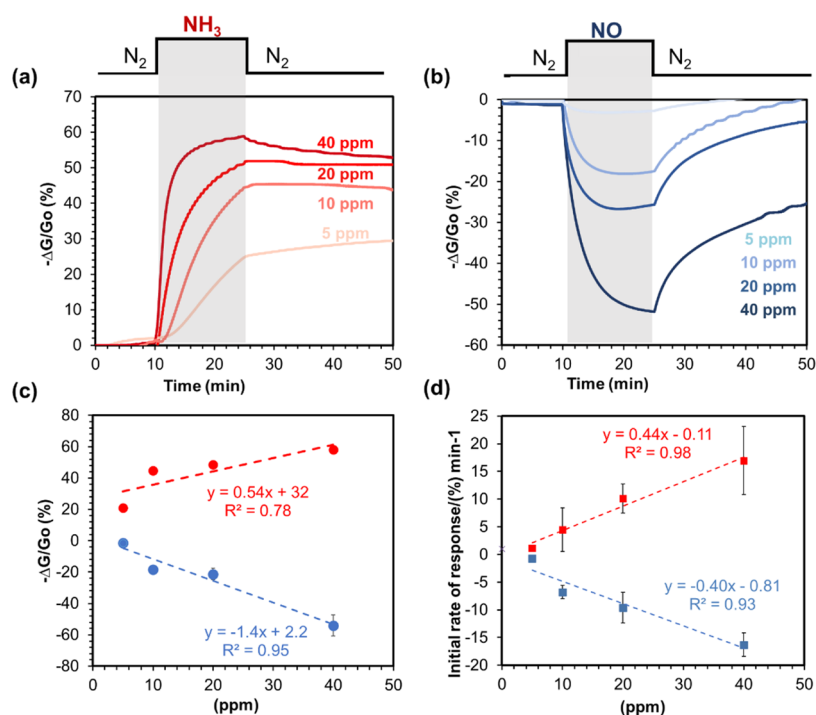
Figure 5. (a) Chemiresistive responses of devices integrated with Bi(HHTP) under an applied voltage of 1.0 V and an atmosphere of dry nitrogen to 15 min of exposure to (a) NH_3 and (b) NO at 40, 20, 10, and 5 ppm. (c) Plot of concentration vs normalized change in conductance ($-\Delta G/G_o$). (d) Initial rate of response as a function of concentration during the first minute of exposure across two gases (NO and NH_3). Error bars represent standard deviations from the mean of responses from three devices.
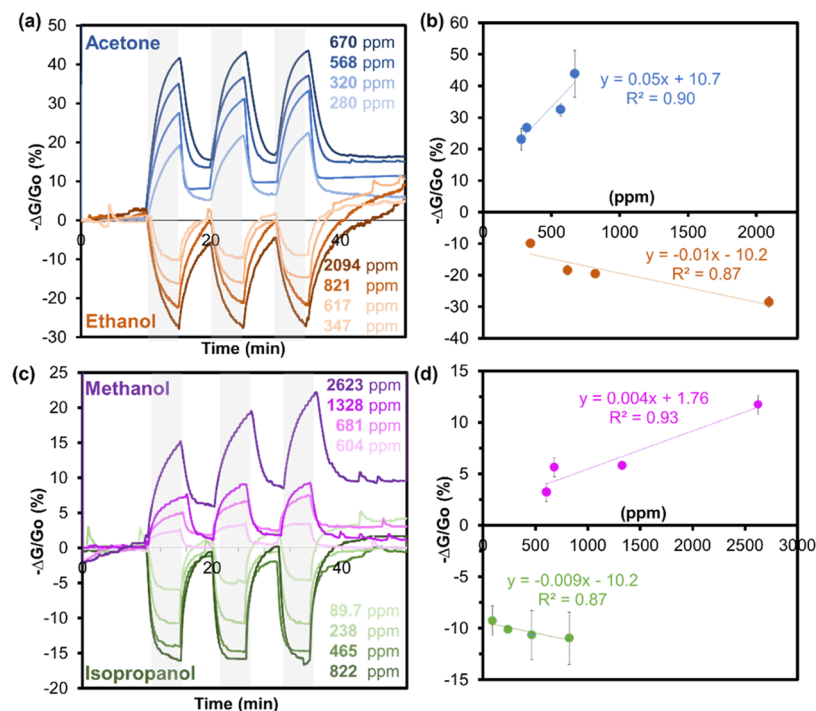

Figure 6. (a) Chemiresistive response of Bi(HHTP) to varying concentrations of acetone (blue) and ethanol (orange) collected at temperatures 25−45 °C. (b) Plot of concentration vs normalized change in conductance ($-\Delta G/G_o$) for exposures to acetone and EtOH. (c) Chemiresistive response of Bi(HHTP) to varying concentrations of MeOH (purple) and iPrOH (green) collected at temperatures 25−45 °C. (d) Plot of concentration vs normalized change in conductance ($-\Delta G/G_o$) for exposures to MeOH and iPrOH. Error bars represent standard deviations from the mean of responses from three devices.

chemiresistive sensing. The favorable semiconductive nature of Bi(HHTP) facilitated the integration of Bi(HHTP) into devices through dropcasting to examine the chemiresistive

response of Bi(HHTP) to the four VOCs (acetone, EtOH, MeOH, and iPrOH) and 40, 20, 10, and 5 ppm of NO and NH_3. Bi(HHTP) exhibited a decrease in conductivity to the
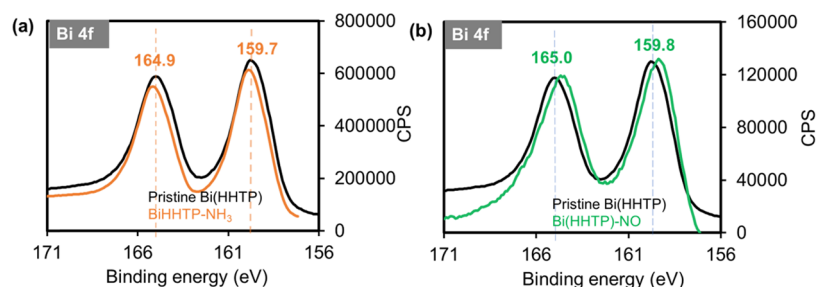
Figure 7. X-ray photoelectron spectroscopy of the (a) Bi $4f_{7/2}$ and the Bi $4f_{5/2}$ region of Bi(HHTP) of pristine and dosed with NH_3 and (b) the Bi $4f_{7/2}$ and the Bi $4f_{5/2}$ region of Bi(HHTP) of pristine and dosed with NO.

reducing gas (NH_3) and an increase in conductivity to the oxidizing gas NO (Figure 5). Upon exposure to 40 ppm of NO, Bi(HHTP) showed a normalized response ($-\Delta G/G_o$) of $-54.8 \pm 6\%$ after 15 min of exposure with excellent reversibility. Also, upon exposure to 40 ppm of NH_3, Bi(HHTP) showed a normalized response ($-\Delta G/G_o$) of $58.4 \pm 2\%$ after the first 15 min of exposure. The observed chemiresistive responses to both oxidizing and reducing gases are thus consistent with the response of a p-type semiconductor.[60] We also examined the response of Bi(HHTP) to NO and NH_3 in the presence of humidity (5000 ppm of H_2O, Figures S40 and S41). We observed a significant decrease in response in the presence of humidity (from -34.4 ± 3.2 to $-19.9 \pm 0.76\%$ $-\Delta G/G_o$) when sensing NO and a considerable increase in response for NH_3 (from 39.6 ± 7.0 to $-81.8 \pm 7.3\%$ $-\Delta G/G_o$) in the same concentration of H_2O. These results may point to the importance of the presence of H-bonding in the sensing mechanism of NH_3.

Bi(HHTP) devices exhibited unique chemiresistive responses toward VOCs that changed in the direction of normalized conductance depending on the analyte (Figure 6). Both MeOH and acetone displayed an increase in normalized conductance ($-\Delta G/G_o$) upon exposure, while EtOH and iPrOH demonstrated a decrease in normalized conductance ($-\Delta G/G_o$) upon exposure to specific concentrations of the analyte. All exposures to the VOCs were observed to be reversible. To better understand the responses and H-bonding interactions of Bi(HHTP) with the four VOCs, we compared the pK_a values, dipole moment, and dielectric constants of each compound (Table S5). The pK_a values of the VOCs increase from MeOH to acetone. While EtOH and iPrOH have similar dipole moments (1.66D), MeOH and acetone have higher dipole moments. Other considerations include the dielectric constants (ε), which decrease down the line from methanol, ethanol, isopropanol, and all the way to the lowest value, acetone. The combination of these electronic and structural properties may explain the observations noted during sensing of VOCs. Furthermore, the presence of water molecules in the pores of Bi(HHTP)-β, as demonstrated by MicroED, may compete as host sites for H-bonding with VOCs. Thus, sensing responses to VOCs may have contributions from two competing mechanisms: one involving Lewis acid and base interactions, and another one involving Brønsted acid or H-bonding interactions with the surface of Bi(HHTP), which we further investigated using several spectroscopic techniques (*vide infra*). I−V curves of Bi(HHTP) during exposure to 1000 ppm of EtOH vapor suggested Ohmic contacts after saturation, excluding the possibility of Schottky barrier modulation mechanism during the sensing of VOCs (Figure S39).

Limits of Detection. To examine the limits of detection (LODs), we focused our attention on two representative biomarkers that are known to be common breath metabolites,[61] acetone and EtOH(*vide infra*). We varied the concentration of these VOCs by increasing the temperature of the chamber housing the analyte from 25 to 40 °C and recorded three sequential exposures (Figure 6). Bi(HHTP) had an average response of $43.8 \pm 7\%$ to 670 ppm of acetone after averaging across three devices exposed for 5 min and recovered in N_2 for 5 min, sequentially. To 2094 ppm of EtOH, Bi(HHTP) has an average response of $-28.5 \pm 2\%$.

To determine the LODs in response to NO and NH_3, we calculated the change in response of Bi(HHTP) upon 15 min of exposure toward NO at different concentrations (5−40 ppm) (for full calculation, see the SI, eqs S7−S9). The theoretical LODs, calculated based on the response after 15 min of exposure to either NO or NH_3 (5−40 ppm), were 0.15 and 0.29 ppm, respectively. These LOD values are comparable to $M_3(HXTP)_2$-based systems,[21,25−28] but do not exceed previously reported MPc-based 2D framework sensitivity to NO.[22] Here, however, Bi(HHTP) displays a unique reversibility to low concentrations of NO (and partial reversibility to concentrations above 20 ppm), as observed by sensing and pXRD experiments (Figures 7 and S53, respectively), that is not observed in either of these previous systems. These reversible sensing characteristics can be particularly advantageous for nanomaterial-based sensors that can be fabricated to withstand repeated exposures to NO for an enhanced long term durability. For VOCs, the LOD values were 41.2 ppm for acetone, 278 ppm for MeOH, 50.2 ppm for iPrOH, and 185 ppm for EtOH. These values are similar to other reported chemiresistive values for alcohol sensors fabricated from metal oxides or reduced graphene oxides.[62] Furthermore, the system we present allows for differentiation between analytes based on the direction of response using a single conductive network. These sensing responses to four VOCs using one conductive network have not been previously observed in chemiresistive sensing. Previously, an array of 2D MOFs was required to distinguish between similar analytes (e.g., MeOH and iPrOH).[19] The unique responses seen in Bi(HHTP) may arise from the interaction of these analytes within the bismuth coordination sphere, offering an exclusive advantage over 2D systems with lower-coordinate metal nodes.

Studies of the Sensing Mechanism with NO and NH_3 Using MicroED, XPS, EPR, ATR-IR, and Diffuse Reflectance Infrared Fourier Transform Spectroscopy (DRIFTS). We first used MicroED to elucidate structural or electronic density changes in Bi(HHTP) induced upon exposure to NO and NH_3 (exposed for 1 h at high concentration, 10 000 ppm or 1% of analyte in N_2). MicroED confirmed that the

coordination network maintained its crystallinity, network topology, and space group upon exposure to the gases (Figures S51 and S52). Gas exposure did, however, induce a slight expansion in unit cell parameters (cell length α and angle β) for both structures of Bi(HHTP) (Figure S51). We hypothesize that this change may have been induced by either occupation of the pores within the coordination network or through structural changes induced by analyte interaction with the host sites within the network. To confirm these structural changes induced by analyte exposure, we utilized pXRD analysis on samples before and after 1 h exposure to 10 000 ppm of NH$_3$ and NO (Figures S52 and S53, respectively). After NH$_3$ exposure, Bi(HHTP) exhibited a significant shift in the peak corresponding to the $(32\bar{1})$ plane. This plane runs parallel to $\pi-\pi$ stacking layers, which suggests that NH$_3$ exposure may be increasing the distances between these planes. This change could result from NH$_3$ occupying the available void volumes within Bi(HHTP) and on the edge sites of the structure, causing the expansion and increase in spacing of these layers. After recovery in N$_2$ for 2 h, this shift did not return to its original position, consistent with our observations in sensing that NH$_3$ induces dosimetric response Bi(HHTP). For NO exposure, we observed a slight shift in the (002), (200), $(20\bar{2})$, and $(32\bar{1})$ planes. These peak shifts partially recover after a 2 h N$_2$ exposure, which is consistent with our observation in sensing that response to NO is partially reversible at concentrations above 20 ppm. These slight deviations in peak position could also indicate NO occupying the available volume within the pores of Bi(HHTP), which is feasible considering the bond length of N−O (1.15 Å), causing increases in distances between Bragg planes.

To gain deeper insight into the changes to the surface chemistry, oxidation states of constituents of Bi(HHTP), and material−analyte interactions, we used X-ray photoelectron spectroscopy (XPS), electron paramagnetic resonance (EPR), DRIFTS, and ATR-IR spectroscopy. XPS was used to confirm the elemental composition of Bi(HHTP), as well as identify chemical shifts typically associated with changes in the population of electronic states. EPR allowed the observation of the effective analyte binding on the location and population of unpaired spins and/or changes in the oxidation state of metal and ligand constituents within the bulk material.[24] In turn, IR techniques provided complementary details regarding the nature of the material−analyte interactions based on changes in the vibrational modes of the participating species.

XPS comparative analysis (carried out at 10^{-9} Torr) was used to analyze the composition of Bi(HHTP) in its pristine state and after exposure to NO and NH$_3$. First, a pristine sample of Bi(HHTP) was purged for 1 h with N$_2$, while another batch was saturated with NO or NH$_3$ (1%, 10 000 ppm) for 1 h and sealed (left for over 24 h as samples were shipped out for analysis, see the SI for details). High-resolution deconvoluted spectra of the C 1s emission line after NO dosing revealed an increase in the peak area assigned to the C−O---Bi binding energy and decrease in the peak area corresponding to the C═O---Bi binding energy (Figure S47b), which supports the hypothesis that the interaction is occurring within the network causing a shift in the chemical environment near the semiquinone/catecholate region. Although not further oxidized, the deconvoluted region of Bi 4f$_{7/2}$ and Bi 4f$_{5/2}$ in the NO-doped Bi(HHTP) displayed a slight shift toward lower binding energies (Figure 7d). This shift may be attributed to electron density transferring from the ligand or bismuth node to NO, causing higher conductivities, less charging, and thus lower binding energies of less tightly bound emitted electrons. We attribute the observations during XPS analysis to be applicable only to the irreversible chemiresistive response to NO. For NH$_3$ exposure, the C 1s region displayed a slight increase in the area corresponding to the C═O---Bi bond (Figure S47c), and in the region corresponding to the C−O---Bi bond. We also observed the presence of a new N 1s peak corresponding to the presence of nitrogen on NH$_3$ adsorbed within the network (Figure S47f). Taken together, XPS data point to significant electronic perturbations near the bismuth metal node, possibly at the catechol region of the ligand after NO/NH$_3$ analyte exposure.

To complement the understanding of material−analyte interactions by XPS and EPR, we employed DRIFTS. Difference spectra were collected upon exposure to 10 000 ppm of each gaseous analyte. After exposure to NO, the presence of negative-going bands at 1255, 860, and 800 cm^{-1} were attributed to the alteration of bismuth-catechol bonding and supported additional spectroscopic data acquired through ATR-IR (Figure S45) of NO interacting at or near the bismuth center, possibly resulting in oxidative damage to the network. After exposure of pristine Bi(HHTP) to 10 000 ppm NH$_3$ followed by purging with N$_2$, positive bands remained at 1250 and 1565 cm^{-1}, which suggested possible chemisorbed NH$_3$ species interacting with Lewis Acid Site (LAS) within the network. Exposure to NH$_3$ caused the appearance of negative going ν(OH) and δ(HOH) bands indicating interactions with or removal of water within the network. Furthermore, we observed varying degrees of reversibility for Bi(HHTP) toward these gaseous analytes; which was quantified by the recovery to the background absorbance after exposure to an analyte and purge with N$_2$ gas (Figures S59 and S60). Bi(HHTP) demonstrated moderate reversibility toward NH$_3$ and no reversibility toward NO at this concentration. This concentration-dependent reversibility for NO-related DRIFTS experiments observed with 10 000 ppm may reflect a different mechanism of sensing and/or active sites at high ppm concentrations of NO compared to low ppm concentrations of NO used for chemiresistive measurements. This possibility appears to be consistent with chemiresistive measurements, which showed decreasing reversibility of response with increasing concentrations of NO. Interestingly, NH$_3$ DRIFTS experiments demonstrated negative-going bands corresponding to either dehydration of the network or disruption of H-bonding within the network; this negative-going water-related response could be related to a decrease in conductivity for NH$_3$ sensing experiments, which would be commensurate with electron donation (i.e., NH$_3$ adsorbing to LAS and Brønsted acid sites [BAS]) onto a p-type semiconductor.

EPR spectroscopy was collected at room temperature in the solid state. EPR analysis of the pristine Bi(HHTP) material displayed a broad absorbance band with low intensity centered at g = 2.000, which indicated that unpaired electron density resided primarily in a ligand-centered orbital or possibly located on adsorbed oxygen molecules. A slight increase in the intensity of the resonant absorbance was observed when the sample was exposed to NO (10,000 ppm for 1 h, Figure S48). This increase in absorbance was also observed for NH$_3$-exposed Bi(HHTP) (10,000 ppm for 1 h, Figure S48). The exposure to NH$_3$ also resulted in a shift of the g-value to g = 1.991. This result suggests that NH$_3$ induced a slight change in

the coordination sphere around the EPR active center, consistent with what is observed at the bismuth site in XPS.

To summarize, XPS and both methods of the infrared analysis indicated that exposure of Bi(HHTP) to NO and NH_3 yielded a significant variation in the electronic state of the ligand and bismuth node. Although the bismuth center was not formally oxidized beyond its pristine state, a shift of the Bi $4f_{7/2}$ and the Bi $4f_{5/2}$ emission lines by XPS analysis indicated a change in electron density surrounding the bismuth node. Due to the strong binding of the analyte NH_3 within the network, we were able to observe the presence of a N 1s peak in the XPS spectrum (Figure S46f). For NO and NH_3, we also observed possible LAS and hydrogen-bonding interactions that were likely accompanied by charge-transfer interactions with the network. DRIFTS experiments for VOC analytes revealed LAS and hydrogen-bonding interactions, with possible protonation/dehydration events occurring within the network. Furthermore, in our DRIFTS experiments, we observed a strong general correlation between negative/positive going water bands for all VOCs and the direction of chemiresistive response. This observation again may point to the importance of H-bonding interactions (either through BAS interactions or change in structural conformations) when considering the mechanism of sensing.

Mechanistic Studies with VOCs Using DRIFTS. Because the VOC analytes in this work showed highly reversible interactions with Bi(HHTP), ex situ analysis by MicroED, XPS, and EPR proved less informative in this context. As such, we turned our attention to the in situ characterization of host–guest interactions between analytes and the coordination network using DRIFTS. This method enabled in situ IR analysis of the solid-state material, while simultaneously permitting analyte exposure, aiding in the elucidation of host–guest interactions (Figures S55–S58). Gas delivery for in situ DRIFTS analysis was handled with a custom-made manifold allowing delivery of vacuum, gas analytes, VOCs, and pure N_2 to purge samples. We observed varying degrees of reversibility for Bi(HHTP) toward VOC analytes; this reversibility was quantified by the recovery to the background absorbance after exposure to an analyte and purge with vacuum. Difference experiments revealed four distinct spectroscopic signatures of VOCs interacting with the network. First, exposure to acetone and EtOH produced negative-going Bi(HHTP) bands within the fingerprint region of the IR spectrum, whereas MeOH and iPrOH did not. Second, negative-going bands corresponding to either dehydration of the network or disruption of hydrogen bonding within the network resulted from exposure to acetone and MeOH. These bands were present in the characteristic water regions (3000 and 1600 cm^{-1}). Third, all of the VOCs were characterized to interact with the network at LAS, most likely at available bismuth sites. Fourth, the background absorbance of Bi-(HHTP) demonstrated high reversibility toward iPrOH and EtOH, moderate reversibility toward MeOH, and partial reversibility toward acetone. These experiments demonstrated that both steric properties of the VOCs (e.g., MeOH versus EtOH) as well as the protic nature of the VOCs (e.g., iPrOH versus acetone) played significant roles in guiding the host–guest interactions at the network interface. We hypothesized that exposure to both MeOH and acetone would result in the depletion of charge carriers (holes) through either electron transfer, H-bonding, or proton-coupled electron-transfer interactions. Bi(HHTP)-β contained water both within the

pores and within the coordination sphere of the bismuth nodes; thus, another possible explanation for the observed sensing responses may be two VOCs interacting through different mechanisms of H-bonding to water molecules and displacing their positions within the pores, triggering a structural change that promotes the mobility of charge carriers within the network. Future studies in transistor device architectures may help clarify the details of material–VOC interactions.

CONCLUSIONS

This report constitutes the first demonstration of a bismuth-based coordination polymer toward chemiresistive sensing. To the best of our knowledge, Bi(HHTP) is among the first HHTP-based network structures solved using electron diffraction techniques.[63] Bi(HHTP) consisted of polyaromatic HHTP ligands interconnected with bismuth metal nodes and exhibited an unprecedented network topology with intricately connected layers, along with good electrical conductivity (5.3 $\times$ 10^{-3} S·cm^{-1}), when compared to other HHTP-based 2D MOFs.[25] Bi(HHTP) can be synthesized at room temperature with environmentally friendly aqueous conditions using a nontoxic metal and relatively inexpensive starting materials. Compared to other reported bismuth-based MOFs that are commonly linked using polyaromatic carboxylate linkers and secondary-building units that exhibit larger pore apertures, Bi(HHTP) adopts a herringbone-like packing (similar to HHTP packing) with slit-shaped pores.

We demonstrate the utility of this material toward chemical sensing of NO and NH_3 with limits of detection of 0.15 and 0.29 ppm respectively, low driving voltages (0.1–1.0 V), and operation at room temperature. The LOD values for NO and NH_3 are like those reported using first-row transition-metal HHTP-based 2D MOF sensors[21,23] and rival that of 2D MOFs made using layer-by-layer liquid-phase epitaxial techniques.[27] Bi(HHTP) is not as sensitive as MPc-based 2D MOFs in response to NO (Table S4).[18,20,22] What is particularly noteworthy is that Bi(HHTP) has a unique, promising selective and reversible response toward NO at concentrations of 20 ppm and below. Although reversible NO binding has been demonstrated in other MOF systems,[64] it has not been observed in chemiresistive sensing using conductive coordination networks. Current limitations of Bi(HHTP) in the context of chemiresistive sensing may be centered on the limited control over the spatial orientation on the surfaces of devices and the thickness of the film may be resolved in the future through further optimization. We also demonstrate the utility of Bi(HHTP) toward sensing four structurally analogous VOCs (acetone, MeOH, EtOH, and iPrOH) to exhibit unique and reversible responses.

This work opens the door to developing a new class of semiconductive crystalline materials using high Z-effective nodes with the ability to accommodate high coordination numbers and adaptable coordination environments. This flexible coordination sphere can permit the examination of structure–property relationships of bismuth-based coordination networks other symmetrical polyaromatic linkers with different heteroatoms. Our work demonstrates that harnessing electronic doping combined with the possibility of H-bonding interactions can lead to unique responses to structurally analogous analytes with similar functional groups (e.g., alcohols) and differences of one hydrogen atom (e.g., EtOH and acetone). Furthermore, advancing the development of

these materials can enable a new class of sensors with ambient operating temperatures, low driving voltages in devices, and enhanced selectivity toward specific analytes for optimized performance.

■ ASSOCIATED CONTENT

Ⓢ Supporting Information

The Supporting Information is available free of charge at https://pubs.acs.org/doi/10.1021/acsami.1c14453.

> BiHHTP_alpha_final_v2 (CIF)
> BiHHTP_beta_final_v3 (CIF)
> BiHHTP_NH3_final_v2 (CIF)
> BiHHTP_NO_final_v3 (CIF)
> Experimental methods, synthetic optimization, material characterization, electronic characteristics, spectroscopic details, crystallographic analysis including the use of MicroED, physical properties, and comprehensive chemiresistive sensing performance and mechanistic data (PDF)

■ AUTHOR INFORMATION

Corresponding Authors

Hosea M. Nelson − *Division of Chemistry and Chemical Engineering, California Institute of Technology, Pasadena, California 91125, United States;* ⓄRCID orcid.org/0000-0002-4666-2793; Email: hosea@caltech.edu

Katherine A. Mirica − *Department of Chemistry, Burke Laboratory, Dartmouth College, Hanover, New Hampshire 03755, United States;* ⓄRCID orcid.org/0000-0002-1779-7568; Email: katherine.a.mirica@dartmouth.edu

Authors

Aylin Aykanat − *Department of Chemistry, Burke Laboratory, Dartmouth College, Hanover, New Hampshire 03755, United States;* ⓄRCID orcid.org/0000-0002-1721-772X

Christopher G. Jones − *Division of Chemistry and Chemical Engineering, California Institute of Technology, Pasadena, California 91125, United States*

Evan Cline − *Department of Chemistry, Burke Laboratory, Dartmouth College, Hanover, New Hampshire 03755, United States*

Robert M. Stolz − *Department of Chemistry, Burke Laboratory, Dartmouth College, Hanover, New Hampshire 03755, United States*

Zheng Meng − *Department of Chemistry, Burke Laboratory, Dartmouth College, Hanover, New Hampshire 03755, United States;* ⓄRCID orcid.org/0000-0002-6775-3213

Complete contact information is available at:
https://pubs.acs.org/10.1021/acsami.1c14453

Notes

The authors declare no competing financial interest.

■ ACKNOWLEDGMENTS

■ REFERENCES

(1) Snyder, E. G.; Watkins, T. H.; Solomon, P. A.; Thoma, E. D.; Williams, R. W.; Hagler, G. S.; Shelow, D.; Hindin, D. A.; Kilaru, V. J.; Preuss, P. W. The Changing Paradigm of Air Pollution Monitoring. *Environ. Sci. Technol.* **2013**, *47*, 11369−11377.

(2) Baron, R.; Saffell, J. Amperometric Gas Sensors as a Low Cost Emerging Technology Platform for Air Quality Monitoring Applications: A Review. *ACS Sens.* **2017**, *2*, 1553−1566.

(3) Ishihara, S.; Azzarelli, J. M.; Krikorian, M.; Swager, T. M. Ultratrace Detection of Toxic Chemicals: Triggered Disassembly of Supramolecular Nanotube Wrappers. *J. Am. Chem. Soc.* **2016**, *138*, 8221−8227.

(4) Lin, C.; Xian, X.; Qin, X.; Wang, D.; Tsow, F.; Forzani, E.; Tao, N. High Performance Colorimetric Carbon Monoxide Sensor for Continuous Personal Exposure Monitoring. *ACS Sens.* **2018**, *3*, 327−333.

(5) Yoo, D. K.; Woo, H. C.; Jhung, S. H. Effective Removal of Particulate Matter from Air by Using Zeolite-Coated Filters. *J. Mater. Chem. A* **2020**, *8*, 17960−17968.

(6) Konvalina, G.; Haick, H. Sensors for Breath Testing: from Nanomaterials to Comprehensive Disease Detection. *Acc. Chem. Res.* **2014**, *47*, 66−76.

(7) Ren, F.; Pearton, S. J. *Semiconductor Device-Based Sensors for Gas, Chemical, and Biomedical Applications*; CRC Press, 2017.

(8) Otagawa, T.; Madou, M.; Wing, S.; Richalexander, J.; Kusanagi, S.; Fujioka, T.; Yasuda, A. Planar Microelectrochemical Carbon-Monoxide Sensors. *Sens. Actuators, B* **1990**, *1*, 319−325.

(9) Wang, C.; Yin, L.; Zhang, L.; Xiang, D.; Gao, R. Metal Oxide Gas Sensors: Sensitivity and Influencing Factors. *Sensors* **2010**, *10*, 2088−2106.

(10) Schroeder, V.; Savagatrup, S.; He, M.; Lin, S.; Swager, T. M. Carbon Nanotube Chemical Sensors. *Chem. Rev.* **2019**, *119*, 599−663.

(11) Yavari, F.; Koratkar, N. Graphene-Based Chemical Sensors. *J. Phys. Chem. Lett.* **2012**, *3*, 1746−1753.

(12) Choi, J. H.; Lee, J.; Byeon, M.; Hong, T. E.; Park, H.; Lee, C. Y. Graphene-Based Gas Sensors with High Sensitivity and Minimal Sensor-to-Sensor Variation. *ACS Appl. Nano Mater.* **2020**, *3*, 2257−2265.

(13) Chen, J.; Chen, Z.; Boussaid, F.; Zhang, D.; Pan, X.; Zhao, H.; Bermak, A.; Tsui, C. Y.; Wang, X.; Fan, Z. Ultra-Low-Power Smart Electronic Nose System Based on Three-Dimensional Tin Oxide Nanotube Arrays. *ACS Nano* **2018**, *12*, 6079−6088.

(14) Zhang, M. L.; Yuan, Z. H.; Song, J. P.; Zheng, C. Improvement and Mechanism for the Fast Response of a Pt/TiO₂ Gas Sensor. *Sens. Actuators, B* **2010**, *148*, 87−92.

(15) Jian, Y. Y.; Hu, W. W.; Zhao, Z. H.; Cheng, P. F.; Haick, H.; Yao, M. S.; Wu, W. W. Gas Sensors Based on Chemi-Resistive Hybrid Functional Nanomaterials. *Nano-Micro Lett.* **2020**, *12*, No. 71.

(16) Xie, L. S.; Skorupskii, G.; Dinca, M. Electrically Conductive Metal-Organic Frameworks. *Chem. Rev.* **2020**, *120*, 8536−8580.

(17) Givaja, G.; Amo-Ochoa, P.; Gomez-Garcia, C. J.; Zamora, F. Electrical Conductive Coordination Polymers. *Chem. Soc. Rev.* **2012**, *41*, 115−147.

(18) Meng, Z.; Aykanat, A.; Mirica, K. A. Welding Metallophthalocyanines into Bimetallic Molecular Meshes for Ultrasensitive, Low-Power Chemiresistive Detection of Gases. *J. Am. Chem. Soc.* **2019**, *141*, 2046−2053.

(19) Campbell, M. G.; Liu, S. F.; Swager, T. M.; Dinca, M. Chemiresistive Sensor Arrays from Conductive 2D Metal-Organic Frameworks. *J. Am. Chem. Soc.* **2015**, *137*, 13780−13783.

(20) Aykanat, A.; Meng, Z.; Benedetto, G.; Mirica, K. A. Molecular Engineering of Multifunctional Metallophthalocyanine-Containing Framework Materials. *Chem. Mater.* **2020**, *32*, 5372−5409.

(21) Ko, M.; Aykanat, A.; Smith, M. K.; Mirica, K. A. Drawing Sensors with Ball-Milled Blends of Metal-Organic Frameworks and Graphite. *Sensors* **2017**, *17*, 2192.

(22) Meng, Z.; Stolz, R. M.; Mirica, K. A. Two-Dimensional Chemiresistive Covalent Organic Framework with High Intrinsic Conductivity. *J. Am. Chem. Soc.* **2019**, *141*, 11929−11937.

(23) Smith, M. K.; Mirica, K. A. Self-Organized Frameworks on Textiles (SOFT): Conductive Fabrics for Simultaneous Sensing, Capture, and Filtration of Gases. *J. Am. Chem. Soc.* **2017**, *139*, 16759−16767.

(24) Stolz, R. M.; Mahdavi-Shakib, A.; Frederick, B. G.; Mirica, K. A. Host−Guest Interactions and Redox Activity in Layered Conductive Metal−Organic Frameworks. *Chem. Mater.* **2020**, *32*, 7639−7652.

(25) Ko, M.; Mendecki, L.; Mirica, K. A. Conductive Two-Dimensional Metal-Organic Frameworks as Multifunctional Materials. *Chem. Commun.* **2018**, *54*, 7873−7891.

(26) Yao, M. S.; Lv, X. J.; Fu, Z. H.; Li, W. H.; Deng, W. H.; Wu, G. D.; Xu, G. Layer-by-Layer Assembled Conductive Metal-Organic Framework Nanofilms for Room-Temperature Chemiresistive Sensing. *Angew. Chem., Int. Ed.* **2017**, *56*, 16510−16514.

(27) Campbell, M. G.; Sheberla, D.; Liu, S. F.; Swager, T. M.; Dinca, M. Cu_3(hexaiminotriphenylene)$_2$: an Electrically Conductive 2D Metal-Organic Framework for Chemiresistive Sensing. *Angew. Chem., Int. Ed.* **2015**, *54*, 4349−4352.

(28) Hmadeh, M.; Lu, Z.; Liu, Z.; Gandara, F.; Furukawa, H.; Wan, S.; Augustyn, V.; Chang, R.; Liao, L.; Zhou, F.; Perre, E.; Ozolins, V.; Suenaga, K.; Duan, X. F.; Dunn, B.; Yamamto, Y.; Terasaki, O.; Yaghi, O. M. New Porous Crystals of Extended Metal-Catecholates. *Chem. Mater.* **2012**, *24*, 3511−3513.

(29) Claire, F. J.; Tenney, S. M.; Li, M. M.; Siegler, M. A.; Wagner, J. S.; Hall, A. S.; Kempa, T. J. Hierarchically Ordered Two-Dimensional Coordination Polymers Assembled from Redox-Active Dimolybdenum Clusters. *J. Am. Chem. Soc.* **2018**, *140*, 10673−10676.

(30) Solomos, M. A.; Claire, F. J.; Kempa, T. J. 2D Molecular Crystal Lattices: Advances in their Synthesis, Characterization, and Application. *J. Mater. Chem. A* **2019**, *7*, 23537−23562.

(31) Claire, F. J.; Solomos, M. A.; Kim, J.; Wang, G.; Siegler, M. A.; Crommie, M. F.; Kempa, T. J. Structural and Electronic Switching of a Single Crystal 2D Metal-organic Framework Prepared by Chemical Vapor Deposition. *Nat. Commun.* **2020**, *11*, No. 5524.

(32) Singh, A. K.; Singh, R. K.; Sharma, B.; Tyagi, A. K. Characterization and Biocompatibility Studies of Lead Free X-ray Shielding Polymer Composite for Healthcare Application. *Radiat. Phys. Chem.* **2017**, *138*, 9−15.

(33) Jin, X. L.; Ye, L. Q.; Xie, H. Q.; Chen, G. Bismuth-Rich Bismuth Oxyhalides for Environmental and Energy Photocatalysis. *Coord. Chem. Rev.* **2017**, *349*, 84−101.

(34) Wang, G.; Sun, Q.; Liu, Y.; Huang, B.; Dai, Y.; Zhang, X.; Qin, X. A Bismuth-Based Metal-Organic Framework as an Efficient Visible-Light-Driven Photocatalyst. *Chem. − Eur. J.* **2015**, *21*, 2364−2367.

(35) Maghrabi, H. A.; Vijayan, A.; Deb, P.; Wang, L. Bismuth Oxide-Coated Fabrics for X-Ray Shielding. *Text. Res. J.* **2016**, *86*, 649−658.

(36) Savage, M.; Yang, S.; Suyetin, M.; Bichoutskaia, E.; Lewis, W.; Blake, A. J.; Barnett, S. A.; Schroder, M. A Novel Bismuth-Based Metal-Organic Framework for High Volumetric Methane and Carbon Dioxide Adsorption. *Chem. − Eur. J.* **2014**, *20*, 8024−8029.

(37) Wibowo, A. C.; Smith, M. D.; zur Loye, H. C. New 3D Bismuth-Oxo Coordination Polymers Containing Terephthalate-Based Ligands: Observation of Bi_2O_2-Layer and Bi_4O_3-Chain Motifs. *CrystEngComm* **2011**, *13*, 426−429.

(38) Norman, N. C. Coordination Chemistry of Antimony and Bismuth: Lewis Acidity, σ^* -Orbitals and Coordination Geometry. *Phosphorus Sulfur Relat. Elem.* **1994**, *87*, 167−176.

(39) Sun, H. Z.; Li, H. Y.; Sadler, P. J. The Biological and Medicinal Chemistry of Bismuth. *Chem. Ber.-/Recl.* **1997**, *130*, 669−681.

(40) Sun, H. *Biological Chemistry of Arsenic, Antimony and Bismuth*; John Wiley & Sons, Ltd, 2010; pp 25−35.

(41) Chapter 2 - Organobismuth(III) Compounds. In *Organobismuth Chemistry*; Suzuki, H.; Matano, Y., Eds.; Elsevier Science: Amsterdam, 2001; pp 21−245.

(42) Wibowo, A. C.; Smith, M. D.; zur Loye, H.-C. A New Kagome Lattice Coordination Polymer Based on Bismuth and Pyridine-2,5-dicarboxylate: Structure and Photoluminescent Properties. *Chem. Commun.* **2011**, *47*, 7371−7373.

(43) Li, K.; Xu, Z.; Xu, H.; Ryan, J. M. Semiconductive Coordination Networks from 2,3,6,7,10,11-Hexakis(alkylthio)-triphenylenes and Bismuth(III) Halides: Synthesis, Structure−Property Relations, and Solution Processing. *Chem. Mater.* **2005**, *17*, 4426−4437.

(44) Inge, A. K.; Koppen, M.; Su, J.; Feyand, M.; Xu, H.; Zou, X.; O'Keeffe, M.; Stock, N. Unprecedented Topological Complexity in a Metal-Organic Framework Constructed from Simple Building Units. *J. Am. Chem. Soc.* **2016**, *138*, 1970−1976.

(45) Li, K.; Xu, H.; Xu, Z.; Zeller, M.; Hunter, A. D. Semiconductive Coordination Networks from Bismuth(III) Bromide and 1,2-bis-(methylthio)phenylacetylene-Based Ligands. *Inorg. Chem.* **2005**, *44*, 8855−8860.

(46) Xu, Z. T.; Li, K. H.; Fettinger, J. C.; Li, J.; King, M. M. A Semiconductive Coordination Network Based on 2,3,6,7,10,11-Hexakis(methylthio)triphenylene and $BiCl_3$. *Cryst. Growth Des.* **2005**, *5*, 423−425.

(47) Mansfield, R. The Electrical Properties of Bismuth Oxide. *Proc. Phys. Soc., B* **1949**, *62*, 476−483.

(48) Luo, Y.-R. *Comprehensive Handbook of Chemical Bond Energies*; CRC Press, 2009; p 66.

(49) Skorupskii, G.; Trump, B. A.; Kasel, T. W.; Brown, C. M.; Hendon, C. H.; Dinca, M. Efficient and Tunable One-Dimensional Charge Transport in Layered Lanthanide Metal-Organic Frameworks. *Nat. Chem.* **2020**, *12*, 131−136.

(50) Miner, E. M.; Wang, L.; Dinca, M. Modular O_2 Electroreduction Activity in Triphenylene-Based Metal-Organic Frameworks. *Chem. Sci.* **2018**, *9*, 6286−6291.

(51) Shi, Y.; Momeni, M. R.; Chen, Y.-J.; Zhang, Z.; Shakib, F. A. Water-Induced Structural Transformations in Flexible Two-Dimensional Layered Conductive Metal−Organic Frameworks. *Chem. Mater.* **2020**, *32*, 9664−9674.

(52) Jones, C. G.; Martynowycz, M. W.; Hattne, J.; Fulton, T. J.; Stoltz, B. M.; Rodriguez, J. A.; Nelson, H. M.; Gonen, T. The CryoEM Method MicroED as a Powerful Tool for Small Molecule Structure Determination. *ACS Cent. Sci.* **2018**, *4*, 1587−1592.

(53) Huang, Z. H.; Grape, E. S.; Li, J.; Inge, A. K.; Zou, X. D. 3D Electron Diffraction as an Important Technique for Structure Elucidation of Metal-Organic Frameworks and Covalent Organic Frameworks. *Coord. Chem. Rev.* **2021**, *427*, No. 213583.

(54) Blatov, V. A.; Shevchenko, A. P.; Proserpio, D. M. Applied Topological Analysis of Crystal Structures with the Program Package ToposPro. *Cryst. Growth Des.* **2014**, *14*, 3576−3586.

(55) Alexandrov, E. V.; Blatov, V. A.; Kochetkov, A. V.; Proserpio, D. M. Underlying Nets in Three-Periodic Coordination Polymers: Topology, Taxonomy and Prediction from a Computer-Aided Analysis of the Cambridge Structural Database. *CrystEngComm* **2011**, *13*, 3947−3958.

(56) Thébault, F.; Ohrstrom, L.; Haukka, M. 2,3,6,7,10,11-Hexahydroxytriphenylene Tetrahydrate: a New Form of an Important Starting Material for Supramolecular Chemistry and Covalent

Organic Frameworks. *Acta Crystallogr., Sect. C: Cryst. Struct. Commun.* **2011**, *67*, o143−5.

(57) Smith, G.; Reddy, A. N.; Byriel, K. A.; Kennard, C. H. L. The Preparation and Crystal Structure of the Bismuth(III) Catecholate Complex Adduct $(NH_4)_2[Bi_2(C_6H_4O_2)_4].(C_6H_6O_2)_2.2H_2O$. *Aust. J. Chem.* **1994**, *47*, 1413.

(58) Guilhaume, N.; Postel, M. Easy Access to Bismuth Catecholates. *Heteroat. Chem.* **1990**, *1*, 233−235.

(59) Guan, H. M.; Zhang, X. D.; Xie, Y. Soft-Chemical Synthetic Nonstoichiometric $Bi_2O_{2.33}$ Nanoflower: A New Room-Temperature Ferromagnetic Semiconductor. *J. Phys. Chem. C* **2014**, *118*, 27170−27174.

(60) Williams, D. E. Semiconducting Oxides as Gas-sensitive Resistors. *Sens. Actuators, B* **1999**, *57*, 1−16.

(61) Diskin, A. M.; Spanel, P.; Smith, D. Time Variation of Ammonia, Acetone, Isoprene and Ethanol in Breath: a Quantitative SIFT-MS Study Over 30 days. *Physiol. Meas.* **2003**, *24*, 107−119.

(62) Boroujerdi, R.; Abdelkader, A.; Paul, R. State of the Art in Alcohol Sensing with 2D Materials. *Nano-Micro Lett.* **2020**, *12*, No. 33.

(63) Leubner, S.; Bengtsson, V. E. G.; Inge, A. K.; Wahiduzzaman, M.; Steinke, F.; Jaworski, A.; Xu, H.; Halis, S.; Ronfeldt, P.; Reinsch, H.; Maurin, G.; Zou, X.; Stock, N. Hexahydroxytriphenylene for the Synthesis of Group 13 MOFs - a New Inorganic Building Unit in a Beta-Cristobalite Type Structure. *Dalton Trans.* **2020**, *49*, 3088−3092.

(64) McKinlay, A. C.; Eubank, J. F.; Wuttke, S.; Xiao, B.; Wheatley, P. S.; Bazin, P.; Lavalley, J. C.; Daturi, M.; Vimont, A.; De Weireld, G.; Horcajada, P.; Serre, C.; Morris, R. E. Nitric Oxide Adsorption and Delivery in Flexible MIL-88(Fe) Metal−Organic Frameworks. *Chem. Mater.* **2013**, *25*, 1592−1599.